RSC Advances

PAPER

View Article Online
View Journal | View Issue

Cite this: *RSC Adv.*, 2026, **16**, 15775

MXene–AuPtPdCu nanoalloy-based aptameric immunosensor for differential pulse voltammetric quantification of colorectal cancer exosomes

Yinzi Yue,[a] Tingting Cui,[b] Meijiao Yao,[c] Huayi Feng,[b] Lianlin Su,[c] Mingming Sun*[b] and Shuai Yan *[b]

This work aims to develop an ultrasensitive electrochemical aptameric immunosensor for quantitative liquid-biopsy detection of colorectal cancer (CRC) exosomes. We engineered a glassy carbon electrode modified with a $Ti_3C_2T_x$ MXene–AuPtPdCu nanoalloy nanocomposite, where uniformly dispersed alloy nanoparticles (8.5 ± 1.2 nm) provide a highly conductive and electrocatalytically active interface, and enable stable immobilization of a thiolated CD63 aptamer *via* Au–S bonding. Exosome capture forms an interfacial blocking layer that hinders $[Fe(CN)_6]^{3-/4-}$ redox probe access, producing a concentration-dependent decrease in differential pulse voltammetry current. Under optimized conditions, the sensor exhibited a linear response from 50 to 5.0 × 10^4 particles μL^{-1} (R^2 = 0.998) with a detection limit of 19 particles μL^{-1}, and delivered 1.8–2.0× signal amplification relative to monometallic MXene-based controls, consistent with the synergistic effects of multicomponent nanoalloys. The platform showed high selectivity against non-target exosomes and serum proteins, good fabrication reproducibility (inter-electrode RSD < 4.5%), and strong storage stability (94.6% signal retention after 28 days at 4 °C). In clinical serum analysis, CRC patients presented significantly elevated exosome levels compared with healthy controls (2.1 × 10^4 *vs.* 0.8 × 10^4 particles μL^{-1}, p < 0.001), and the results agreed well with a commercial ELISA (R^2 = 0.995). These findings demonstrate that MXene-supported AuPtPdCu nanoalloy interfaces can substantially enhance aptamer-based electrochemical exosome quantification, offering a sensitive and reliable strategy for CRC-related liquid biopsy.

Received 15th February 2026
Accepted 16th March 2026

DOI: 10.1039/d6ra01343k

rsc.li/rsc-advances

1. Introduction

Colorectal cancer (CRC) remains a major global health burden, and patient outcomes are strongly tied to disease stage at diagnosis. Late presentation is common and is a key driver of CRC mortality, whereas earlier detection enables more effective intervention and improved survival.[1] Current clinical pathways rely heavily on colonoscopy and related procedures, which are accurate but invasive, costly, and difficult to deploy at population scale for frequent screening.[2] These limitations have accelerated interest in minimally invasive liquid biopsy strategies that measure tumor-associated biomarkers in accessible body fluids.[3] Among liquid biopsy candidates, extracellular vesicles (EVs), particularly exosomes (typically ~30–150 nm), have attracted strong attention because they are released by most cell types, are stable in circulation, and carry proteins and nucleic acids that reflect the physiological state of the parental cells.[4] In CRC, tumor-associated EVs/exosomes have been increasingly linked to early detection and disease monitoring, and recent clinical and translational studies further support the diagnostic value of exosome-derived signatures.[5] A central analytical goal is therefore the sensitive and reliable quantification of CRC-relevant exosomes in complex matrices such as serum.[6]

However, exosome quantification remains technically challenging. Clinically relevant samples often contain low target abundance, substantial heterogeneity, and high backgrounds of proteins and non-target vesicles.[7] Conventional approaches such as nanoparticle tracking analysis, transmission electron microscopy, and immunoblotting are informative but are generally limited by throughput, instrumentation burden, and/or quantification practicality in routine testing workflows.[8] Immunoassays such as ELISA provide convenient quantification, yet they can struggle to resolve small concentration differences that may be important for early-stage disease, particularly in high-background biofluids.[9,10] The tetraspanin protein CD63, highly abundant on the surface of many exosomes, serves as a canonical exosomal marker and a valuable

[a]*Department of General Surgery, Suzhou TCM Hospital Affiliated to Nanjing University of Chinese Medicine, Suzhou, Jiangsu, 215009, China*

[b]*Department of Anorectal Surgery, Suzhou TCM Hospital Affiliated to Nanjing University of Chinese Medicine, Suzhou, Jiangsu, 215009, China. E-mail: 20077840@qq.com; doctor_shuaiyan@njucm.edu.cn*

[c]*School of Pharmacy, Nanjing University of Chinese Medicine, Nanjing, 210023, Jiangsu, China*

target for their capture and detection.[11,12] Together, these constraints define a clear need for rapid, cost-effective, and ultrasensitive sensing platforms that maintain specificity under real-matrix conditions.[13]

Electrochemical biosensors have the advantages of high sensitivity, fast response speed, low cost, great miniaturisation potential, simple operation, *etc.*, and have become a powerful alternative technology.[14–16] The effectiveness of these sensors largely depends on how the electrode interface is designed. This interface must use materials that can accurately identify the target analyte while also converting the binding interaction into a clear and measurable electrical signal.[17] In this setting, two-dimensional nanomaterials—especially $Ti_3C_2T_x$ MXene—have attracted considerable attention because of their metallic conductivity, hydrophilic surface terminations, and large accessible surface area.[18] $Ti_3C_2T_x$ MXene belongs to a family of two-dimensional transition-metal carbides/nitrides bearing surface terminations such as –O, –OH, and –F, which facilitate biomolecule interfacing and rapid interfacial electron transport. At the same time, $Ti_3C_2T_x$ is not indefinitely stable in oxygenated aqueous media and can gradually oxidize to TiO_2-rich species, with degradation reported to be faster in liquid dispersions than in solid-state forms.[19–21] Therefore, practical MXene-based biosensors require careful control of storage, processing time, and interfacial assembly conditions.[22,23] In the present work, freshly prepared MXene was used for composite fabrication, and the sensing interface was ultimately operated as a solid electrode coating rather than as a long-term aqueous colloid, which helps mitigate—but does not fully eliminate—the impact of MXene oxidation.[24] To further increase signal output and overall sensing performance, noble metal nanomaterials are often incorporated. Among these, high-entropy nanoalloys (HENAs), which consist of four or more main elements in nearly equal proportions, have emerged as an important new material system.[25] Compared with monometallic or bimetallic nanoparticles, HENAs usually show stronger catalytic activity and better stability, which is driven by synergy, lattice distortion and the so-called cocktail effect.[26] We hypothesize that decorating $Ti_3C_2T_x$ MXene nanosheets with an equimolar AuPtPdCu multi-metal nanoalloy can create a nanocomposite with simultaneously optimized biofunctional anchoring and interfacial electrochemical kinetics. Au was intentionally introduced to enable robust Au–S bonding with the thiolated CD63 aptamer, a widely used stng stable and reproducible nucleic-acid interfaces on noble-metal surfaces.[27,28] Pt and Pd were selected as catalytically active and chemically stable noble metals that can accelerate interfacial charge transfer, while Cu was incorporated as a 3d component that modulates the electronic structure and lattice strain of noble-metal lattices, which is frequently reported to enhance activity and durability in alloy electrocatalysts.[29] More broadly, multi-principal-element/high-entropy nanoalloys can exhibit 'cocktail-effect' synergy and lattice distortion that tune adsorption energetics and charge redistribution, thereby improving electrochemical performance compared with single-metal nanoparticles.[30]

In this study, we reported on the design and manufacture of a new electrochemical induction sensor for sensitive and selective quantification of CRC-derived exosome.[31] The sensor is built on a glass-carbon electrode (GCE) modified by $Ti_3C_2T_x$ MXene–AuPtPdCu nanoalloy (MXene–NAs) nanocomposite. Then the exosome surface protein CD63-specific tero-modified DNA adaptor was fixed on the surface of MXene–NAs.[32] Binding of CRC exosomes onto the aptamer-functionalized interface reduces the faradaic DPV signal of the $[Fe(CN)_6]^{3-/4-}$ probe primarily through interfacial blocking, including steric exclusion of probe access and an increase in the electron-transfer barrier at the electrode surface. Because both the DNA phosphate backbone and exosome membranes are negatively charged, an additional electrostatic contribution to suppression of the anionic redox probe may also be present; accordingly, the measured current decrease reflects a combined interfacial effect rather than a purely steric process.[33] The magnitude of signal decay increases with the amount of captured exosomes and is used for quantitative analysis. We have comprehensively characterised the synthesised nanocomposites and systematically evaluated the analytical performance of the sensor, including its sensitivity, selectivity, repeatability, stability and application in clinical serum samples. This study aims to propose a new liquid biopsy diagnostic method by combining the complementary advantages of MXenes and high entropy nanoalloys to make early detection of colorectal cancer possible.

2. Materials and methods

2.1 Chemicals and reagents

Titanium aluminum carbide (Ti_3AlC_2, 400 mesh, 98%) powder comes from Laizhou Kaine Ceramic Materials Co., Ltd. Hydrofluoric acid (40% HF), hydrochloric acid (37% HCl), chloric acid ($HAuCl_4 \cdot 3H_2O$, 99.9%), hexahydrate platinum chloride ($H_2PtCl_6 \cdot 6H_2O$, 99.9%), palladium chloride (ii) ($PdCl_2$, 99%), copper chloride (ii) ($CuCl_2$, 99%), sodium borohydride ($NaBH_4$, 99%), potassium iron cyanide ($K_3[Fe(CN)_6]$) and potassium trihydrate ferrocyanide ($K_4[Fe(CN)_6] \cdot 3H_2O$) purchased from Sigma-Aldrich (MO. Louis). Sangong Biotechnology Co., Ltd (Shanghai, China)[11] synthesised a 5′ base modifier targeting cd63 (5′-sh-(CH_2) 6-taaccacccctccgctcccgtgacactaatgctaattcc Aa-3′). Obtained phosphate buffered saline (PBS, pH 7.4) and serum albumin (BSA) from Sigma-Aldrich. All aqueous solutions are prepared by deionised water (18.2 MΩ cm) produced by Millipore purification system (Millipore, USA).

2.2 Synthesis of delaminated $Ti_3C_2T_x$ MXene nanosheets

Multilayer Ti_3C_2T were prepared by selectively removing the Al layer on the Ti_3AlC_2MAX precursor. Simply put, 2.0 g of Ti_3AlC_2 powder was continuously magnetically stirred in a Teflon container and gradually added to 40 mL of 40% HF. The etching reaction was carried out at 40 °C for 48 hours. Subsequently, the suspension was repeatedly washed with deionized water and centrifuged (at 3500 rpm for 5 minutes) until the pH value of the supernatant reached approximately 6. The sediment collected corresponds to multiple layers of Ti_3C_2T youdaoplaceholder0 and is stratified. Disperse the material in 100 mL of deionized water and ultrasonically treat it in an ice bath under an argon

atmosphere for 1 hour. Then, centrifuge the dispersion at 3500 rpm for 1 hour to remove the unstripped fragments. Carefully collect the dark-green supernatant containing delaminated $Ti_3C_2T_x$ nanosheets and store it at 4 °C for short-term use. Because $Ti_3C_2T_x$ is known to oxidize gradually in aqueous dispersions, especially in the presence of dissolved oxygen, the MXene dispersion was used as freshly as possible for subsequent nanocomposite preparation rather than for long-term storage. The concentration of Ti_3C_2T youdaoplaceholder0 dispersion is quantified by drying a known volume and weighing the remaining solid.

2.3 Synthesis of $Ti_3C_2T_x$ MXene–AuPtPdCu nanoalloy (MXene–NAs) nanocomposite

MXene–NAs nanocomposites were prepared by a one-step aqueous co-reduction method. Specifically, first ultrasonically treat 50 mL of Ti_3C_2T youdaoplaceholder1 dispersion (1.0 mg mL^{-1}) for 30 minutes to obtain a uniform suspension. Then, under vigorous stirring, the metal salt solution is added to the MXene dispersion. Based on the previous optimization results,[34] 250 microliters of tetrachloroauric acid, hexachloroplatinic acid, palladium chloride and copper chloride solutions with concentrations of 10 millimoles each were added in sequence. Stir the mixture for 1 hour to promote the adsorption of metal ions onto negatively charged MXene sheets. Next, quickly add 5 milliliters of freshly prepared ice bath sodium borohydride solution (50 mM). The solution immediately changes from green to black, indicating that metal ions undergo reduction and form nanoalloys. After reacting at room temperature for 3 hours, the Mxene–NAs composites were collected by centrifugation (10 000 rpm for 15 minutes). Because the four metal precursors are pre-adsorbed on the same MXene surface and reduced in a single, rapid co-reduction step, co-nucleation is favored over sequential deposition, which helps suppress core–shell growth. Rapid, high-driving-force synthesis routes have been widely reported to yield single-phase solid-solution high-entropy alloy nanoparticles when multiple precursors are reduced together. The product was washed three times with deionized water to remove residual reagents, and then re-dispersed in 5 mL of deionized water to obtain a stable reserve suspension with a concentration of 10 mg mL^{-1}. For the control samples, the synthesis of Mxene–Au, MXene–PT and Mxene–PD followed the same process, but only the corresponding single metal precursors were used.

2.4 Fabrication of the aptasensor

Before modification, polish GCE with 1.0, 0.3 and 0.05 μm alumina slurry on the polishing cloth in turn, and then ultrasound in ethanol and deionised water for 5 minutes each. The cleaned electrodes are dried under the high-purity nitrogen flow. In order to make a sensing interface, 5 μL MXene–NAs suspension (1.0 mg mL^{-1}) is cast to the GCE surface and dried at room temperature. Then gently rinse the electrode with deionised water to remove any loosely bound substances to obtain MXene–NAs/GCE. In order to fix the adaptor, MXene–NAs/GCE was incubated in PBS (pH 7.4) at 4 °C for 12 hours in a 1.0 μM thiol-modified CD63 lind solution. In nanoalloys,[28] the group forms a stable Au–S covalent bond with the Au atom. After incubation, rinse the electrode with PBS to remove the non-specifically bound suitable body. In order to block any remaining active sites and reduce non-specific binding, the electrode (Apt/MXene–NAs/GCE) is incubated in a 1 mm 6-myl-1-hexanol (MCH) solution for 1 hour, and then rinsed with PBS. The prepared lid sensor is stored at 4 °C when not in use.

Before surface modification, the glassy carbon electrode (GCE) was polished successively on a polishing pad with 1.0, 0.3 and 0.05 μm alumina slurry, and then ultrasonically cleaned in ethanol and deionized water for 5 minutes respectively. After cleaning, dry the electrodes through a high-purity nitrogen gas flow. To construct the sensing layer, 5 μL of MXene–NAS suspension (1.0 mg mL^{-1}) was dropped onto GCE and dried at room temperature. The electrode was gently rinsed with deionized water to remove the loosely adhering substances, and MXene–NAs/GCE was obtained. For the fixation of the aptamer, the modified electrode was immersed in a 1.0 μM thiol-functionalized CD63 aptamer solution prepared in PBS (pH 7.4) and incubated at 4 °C for 12 hours. In this step, the thiol group firmly binds to the Au atoms in the nanoalloy through the Au–S covalent interaction.[28] After the incubation step, the electrodes are rinsed with PBS to remove excess aptamers and those that bind in a non-specific manner. To seal the unoccupied surface sites and reduce non-specific adsorption, the electrode (Apt/MXene–NAS/GCE) was further treated with 1 mM 6-mercapto-1-hexanol (MCH) for 1 hour, and then rinsed with PBS. The assembled aptamer sensor should be stored at 4 °C when not in use.

2.5 Electrochemical measurements and exosome detection

A GCE disk served as the working electrode (3.0 mm diameter; geometric area = 0.071 cm^2), a platinum wire was used as the counter (auxiliary) electrode, and an Ag/AgCl reference electrode (3 M KCl filling solution) was employed. In a solution of 5.0 mM $[Fe(CN)_6]^{3-/4-}$ containing 0.1 M KCl, CV and EIS were used to electrochemically characterise each modification step. CV scanning is carried out at a scanning rate of 50 mV s^{-1}. EIS measurement is carried out in the frequency range of 0.1 Hz to 100 kHz, and the AC amplitude is 5 mV under the formal potential of the redox probe. For exosome detection, the prepared aptasensor was incubated with CRC-derived exosomes isolated either from colorectal cancer cell-culture supernatants or from human serum samples. Exosome isolation and characterization are described in Section 2.X. Exosome concentrations were determined by nanoparticle tracking analysis and are reported as particles per μL. The aptasensor was incubated with the target exosome suspension in PBS (pH 7.4) at 37 °C for 60 min, followed by gentle washing with PBS before DPV measurement. After incubation, rinse the electrode with PBS to remove the unbound exosome. Then DPV is measured in the same $[Fe(CN)_6]^{3-/4-}$ solution. DPV parameter optimisation is set to: pulse amplitude 50 mV, pulse width 50 ms, step potential 5 mV.[35,36] The change of DPV peak current ($\Delta I = I_0 - I$) is used as an analysis signal, where I_0 is the initial peak current before exosome incubation, and I is the peak current after incubation.

Cyclic voltammetry was performed at a scanning rate of 50 mV s^{-1}. Electrochemical impedance spectroscopy tests were conducted within the frequency range of 0.1 Hz to 100 kHz, with an alternating current disturbance of 5 mV applied at the formal potential of REDOX pairs. When conducting exosome analysis, the prepared aptamer sensor was incubated with different concentrations of colorectal cancer exosomes (taken from cell culture supernatants or patient serum) in PBS (pH 7.4) at 37 °C for 60 minutes. Then rinse the electrode with electrode buffer to remove unbound exosomes. Then the differential pulse voltammetry (DPV) curves were recorded in the same $[Fe(CN)_6]^{3-/4-}$ electrolyte. The conditions of differential pulse voltammetry were optimized and set as a pulse amplitude of 50 mV, a pulse width of 50 ms, and a step potential of 5 mV.[35,36] The variation of peak current in differential pulse voltammetry (defined as $\Delta I = I_0 - I$) is used as the quantitative response signal.

3. Results and discussion

3.1 Synthesis and characterization of the MXene–NAs nanocomposite

The successful manufacture of high-performance electrochemical sensors depends on the precise synthesis and morphological control of the nanomaterials that make up them. In this work, the sensing platform is built upon a novel nanocomposite of $Ti_3C_2T_x$ MXene decorated with AuPtPdCu high-entropy nanoalloys. A wide range of analytical methods are employed to confirm the structure, morphology, chemical composition and crystallinity of synthetic materials.

Fig. 1 shows the morphological characteristics of the synthesized layered $Ti_3C_2T_x$ nanosheets. The SEM image (Fig. 1A) reveals a characteristic accordion-like, layered structure, which is a hallmark of successfully etched MAX phase powders. After delamination *via* sonication, the TEM image (Fig. 1B) shows large, transparent, and sheet-like structures, confirming the exfoliation of the bulk material into thin nanosheets with lateral dimensions of several micrometers. The wrinkled and flexible appearance is typical for 2D materials prepared by liquid-phase exfoliation.[37]

To further confirm the successful synthesis and exfoliation, XRD analysis was conducted (Fig. 2A). The XRD profile of the original Ti_3AlC_2 MAX phase displays several well-defined diffraction peaks, with the strongest signal appearing at 39.0°, which is assigned to the (104) plane. Following HF treatment,

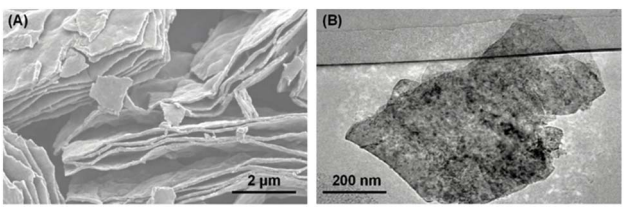

Fig. 1 Morphological characterization of $Ti_3C_2T_x$ MXene. (A) SEM image of multi-layered $Ti_3C_2T_x$ after HF etching. (B) TEM image of delaminated, few-layered $Ti_3C_2T_x$ nanosheets.

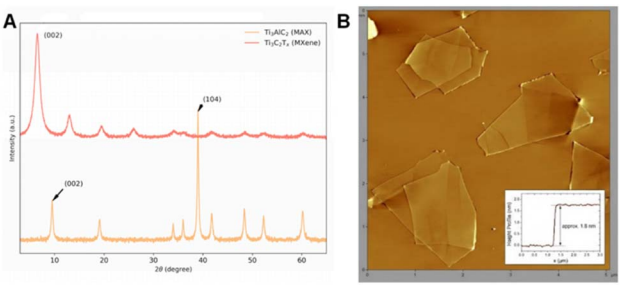

Fig. 2 (A) The XRD spectrum of the precursor Ti_3AlC_2MAX phase and the synthesised $Ti_3C_2T_x$ MXene, the MAX phase peak disappears, and the (002) peak characteristic displacement is small. (B) AFM image of stripping $Ti_3C_2T_x$ nanofilm on the mica substrate.

the typical diffraction features of Ti_3AlC_2, including the prominent (104) reflection, were no longer observed, indicating successful removal of the Al layer. A new prominent peak emerged at a much lower 2θ value of 6.5°, which is assigned to the (002) plane of $Ti_3C_2T_x$. The (002) peak decreased from ~9.5° in the MAX phase to 6.5°, indicating that the *c* lattice parameter has increased significantly from 18.6 to 27.2 Å. The increase in interlayer distance is due to the elimination of the Al layer and the insertion of water molecules and surface groups such as –OH and –F in the etching process, thus confirming the effective conversion of the MAX phase into Mxene.[20,21] Use an atomic force microscope to detect the thickness of the stripped nanofilm. As shown in Fig. 2B, the representative AFM image of $Ti_3C_2T_x$ deposited on the mica substrate shows sheet-like characteristics consistent with the TEM results. The height profile shows that the thickness of a single nanochip is about 1.8 nm, which is very consistent with the expected thickness (~1 nm) of a single $Ti_3C_2T_x$ layer when considering the contribution of the surface end and adsorption water.[5] These observations verify effective exfoliation into single- or few-layer nanosheets, a key factor for increasing surface area and offering plentiful anchoring sites for subsequent nanoalloy growth.[38,39]

The morphology of MXene–AuPtPdCu (MXene–NAs) nanocomposites was characterised by TEM (Fig. 3). As shown in Fig. 3A, on the surface of the relatively bright and transparent MXene nanochip, dark nanoparticles are evenly and densely distributed, and obvious aggregation is rarely observed. This uniform distribution is mainly due to the fact that the abundant

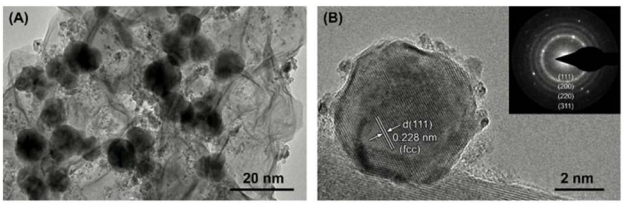

Fig. 3 (A) Low-magnification TEM image of the MXene–AuPtPdCu nanocomposite, showing uniform dispersion of nanoalloys on the MXene support. (B) HRTEM image of a single AuPtPdCu nanoalloy, displaying clear lattice fringes corresponding to the fcc (111) plane. The inset shows the SAED pattern.

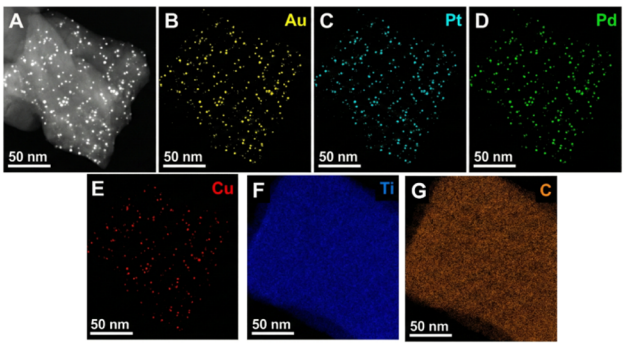

Fig. 4 (A) HAADF-STEM image of the MXene–AuPtPdCu nanocomposite. (B–G) EDX maps of Au, Pt, Pd, Cu, Ti, and C confirm nanoalloy formation and distribution on the MXene sheet.

surface functional groups on MXene provide effective anchor positioning points for metal precursor ions, enabling them to be reduced *in situ*.[40,41] The statistical analysis of more than 100 particles shows that the average diameter of nanoalloys is 8.5 ± 1.2 nm. The HRTEM image shows further structural information (Fig. 3B). The lattice stripe with a surface spacing of 0.228 nm is clearly observed, which corresponds to the (111) surface of the face-centred cubic (fcc) structure.[42] It is worth noting that this spacing falls between the (111) surfaces of pure Au, Pt, Pd and Cu, indicating the formation of a uniform alloy, not a physical mixture of individual metal nanoparticles.[34] In addition, the selective region electron diffraction (SAED) diagram shown in Fig. 3B shows obvious polycrystalline rings corresponding to the (111), (200), (220) and (311) planes of the fcc structure, which further confirms the successful synthesis of crystal nanoalloys.

To verify the elemental composition and spatial distribution of the nanoalloys on the MXene support, HAADF-STEM and EDX mapping were performed (Fig. 4). The HAADF-STEM image (Fig. 4A), where the brightness is proportional to the atomic number (Z-contrast), clearly shows the high-Z nanoalloys as bright spots against the darker MXene background. The corresponding EDX maps (Fig. 4B–E) demonstrate a perfect overlap in the spatial distribution of Au, Pt, Pd, and Cu, providing compelling evidence that these elements are co-located within the same nanoparticles, thus confirming the formation of a quinary nanoalloy structure. The maps for Ti and C (Fig. 4F and G) show their distribution across the entire area, consistent with the underlying MXene support. Quantitative EDX analysis (Table 1) shows that the atomic fractions of Au, Pt, Pd, and Cu are 24.1%, 25.8%, 25.3%, and 24.8%, respectively. These values closely match the equimolar ratio of metal precursors employed during synthesis.[43] We note that area EDX mapping primarily supports co-localization at the nanometre scale and may not fully exclude a very thin segregated shell because of the intrinsic spatial-resolution limits of X-ray signal generation in nanoparticles.

Table 1 Elemental composition of the AuPtPdCu nanoalloys on $Ti_3C_2T_x$

Element	Precursor molar ratio (%)	Atomic% (from EDX)	Atomic% (from XPS)
Au	25.0	24.1	23.8
Pt	25.0	25.8	26.1
Pd	25.0	25.3	25.5
Cu	25.0	24.8	24.6

Table 2 EIS fitting parameters for each electrode modification step, including solution resistance, charge-transfer resistance, and constant phase element parameters

Electrode	(R_s) (Ω)	(R_{ct}) (Ω)	(Q) ($\times 10^{-5}$) S s(^{n}))	(n)
Bare GCE	21.4	350.2	8.9	0.90
MXene–NAs/GCE	19.8	45.1	24.0	0.88
Apt/MXene–NAs/GCE	20.7	851.6	13.0	0.86
Exo/Apt/MXene–NAs/GCE	22.1	2603.5	7.1	0.84

Analyse the crystal structure of MXene–NAs composite materials with XRD correspondence, and show the characteristic peak of $Ti_3C_2T_x$ at 6.3° (002), slightly shifted from the pristine MXene, which may be due to the interaction with the nanoalloys. In addition to the MXene peak, a broad diffraction peak is observed at $2\theta = 39.8°$. This peak can be attributed to the (111) reflection of the fcc structure of the AuPtPdCu nanoalloy. Au, Pt, Pd or Cu do not have separate peaks, but there are single, wide alloy peaks, indicating the formation of a solid solution alloy structure.[44,45] The lattice parameter calculated by the diffraction peak is 3.96 Å, which is between the constituent metals, which is in line with the Vigard law of the alloy system. In addition, the obvious peak width reflects the small grain size of the nanoalloy. According to the Scherrer equation, the grain size is estimated to be about 8.1 nm, which is consistent with the grain size obtained by TEM analysis. The surface composition and chemical state of MXene–NAs composite materials

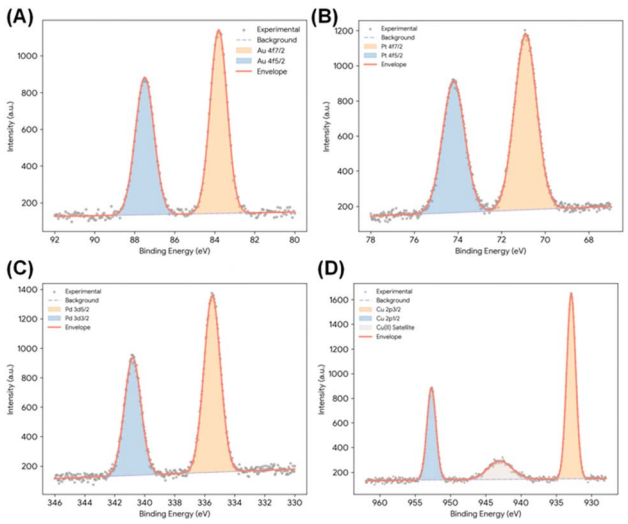

Fig. 5 The high-resolution XPS spectrum of MXene–AuPtPdCu nanocomposite shows (A) Au 4f, (B) Pt 4f, (C) Pd 3d and (D) Cu 2p regions. The spectrum mainly reflects the metallic state and clearly reflects the electronic interaction between the constituent elements, which supports the formation of uniform alloys.

were studied using X-ray photoelectron energy spectrum (XPS). The wide scanning spectrum shows clear signals of Ti, C, O, F, Au, Pt, Pd and Cu, and no other impurity elements were observed. The detection of O and F is expected because these elements come from the surface end of $Ti_3C_2T_x$ produced during HF etching. The quantitative element composition obtained by XPS is shown in Table 2, which is consistent with the EDX analysis results, which further verifies the expected successful formation of composite materials. In order to obtain more detailed information on the internal electronic structure of nanoalloys and the interaction between elements, we further analysed the high-resolution XPS spectrum, as shown in Fig. 5. The Au 4f spectrum (Fig. 5A) can be inversely convolutioned into two peaks of 83.8 eV (Au $4f_{7/2}$) and 87.5 eV (Au $4f_{5/2}$), corresponding to the metal Au(0). These values show a negative displacement compared with the volume Au (84.0 eV), indicating that Au atoms gain electrons from more electropositive Cu and Pd atoms.[46,47] Similarly, the Pt 4f spectrum (Fig. 5B) shows two characteristic peaks, 70.9 eV (Pt $4f_{7/2}$) and 74.2 eV (Pt $4f_{5/2}$) respectively. Compared with the body Pt (71.2 eV), the binding energy of the two peaks is slightly reduced, indicating that there is electronic interaction inside the alloy. In contrast, the Pd 3d spectrum (Fig. 5C) presents Pd(0) signals at 335.5 eV (Pd $3d_{5/2}$) and 340.8 eV (Pd $3d_{3/2}$), and they transfer to higher binding energy relative to the body Pd (335.1 eV). The Cu 2p spectrum (Fig. 5D) is characterised by the peaks of Cu(0) at 932.9 eV (Cu $2p_{3/2}$) and 952.7 eV (Cu $2p_{1/2}$). In addition, weak satellite features are observed, indicating a small degree of surface oxidation to Cu(II), a phenomenon commonly reported for copper-based nanoparticles. The binding energy of Cu(0) is also positively shifted compared to bulk Cu (932.6 eV). These shifts in binding energies are a hallmark of charge redistribution and strong electronic interactions among the constituent metals, providing definitive proof of alloy formation at the atomic level. These trends are consistent with alloying-related electronic interaction and charge redistribution among the constituent metals (initial-state effects). At the same time, we acknowledge that for small supported nanoparticles, measured BE shifts can also include final-state contributions arising from differences in core–hole screening/relaxation that depend on particle size, morphology, and the local dielectric environment. Therefore, the observed shifts are most appropriately interpreted as predominantly reflecting alloying-induced electronic interaction, with possible partial contributions from nanoscale final-state screening effects. Importantly, alloy formation in our material is supported not only by XPS but also by the intermediate fcc(111) lattice spacing in HRTEM, the single broad fcc(111) diffraction feature in XRD without separate monometallic peaks, and the strong spatial overlap of Au/Pt/Pd/Cu in STEM–EDX mapping, collectively indicating a solid–solution nanoalloy rather than a physical mixture. The concurrent core-level shifts in Au/Pt/Pd/Cu further support an electronically coupled alloyed state, which would be less expected for strongly segregated multi-domain particles.[48]

The chemical state of the MXene support was also examined (Fig. 6). The Ti 2p spectrum (Fig. 6A) is complex, showing multiple components corresponding to Ti–C bonds (455.0 eV), Ti^{2+} (456.1 eV), Ti^{3+} (457.3 eV), and a small amount of TiO_2 (458.8 eV) from surface oxidation. The C 1s spectrum (Fig. 6B) can be decomposed into C-ti (281.8 eV), C–C (284.8 eV), C–O (286.5 eV) and O–C=O (288.9 eV). These characteristics are typical of $Ti_3C_2T_x$ MXene and indicate that the basic MXene framework is largely preserved after nanoalloy deposition. We note that the Ti 2p spectrum also contains a minor TiO_2-related contribution, which is consistent with the limited surface oxidation commonly reported for $Ti_3C_2T_x$ during aqueous processing. However, the persistence of Ti–C/C–Ti signals together with the low R_{ct} of MXene–NAs/GCE and the stable sensing response over 28 days indicates that such oxidation remains limited and does not compromise the functional role of the MXene support within the timescale of this study.[49]

Use Raman spectroscopy to detect the vibration characteristics of the material (Fig. 7A). The original $Ti_3C_2T_x$ shows a typical Raman band at about 200 370 and 620 cm^{-1}, which is caused by the vibration of Ti, C and the surface terminal base.[50] After loading the AuPtPdCu nanoalloy, the position of these strips changed slightly, and the relative strength also changed. This change is characterised by the surface-enhanced Raman scattering (SERS) effect caused by the local surface plasma resonance of precious metal nanoparticles. This behaviour reflects the strong electron coupling between nanoalloys and MXene carriers, which is conducive to charge transfer and electrochemical applications.[51,52]

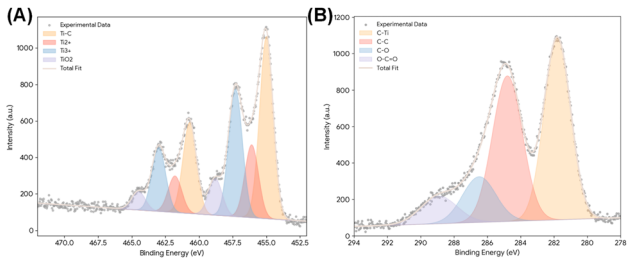

Fig. 6 High-resolution XPS spectra of the MXene–AuPtPdCu nanocomposite showing the (A) Ti 2p and (B) C 1s regions, which confirm the characteristic chemical states of the $Ti_3C_2T_x$ MXene support.

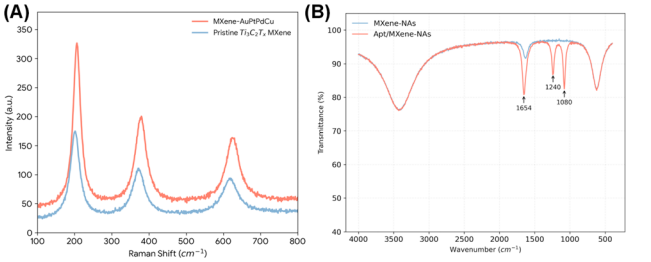

Fig. 7 (A) Raman spectra of pristine $Ti_3C_2T_x$ MXene and the MXene–AuPtPdCu nanocomposite, showing peak shifts and intensity changes indicative of electronic coupling. (B) FTIR spectra of the MXene–NAs composite and the aptamer-modified MXene–NAs (Apt/MXene–NAs) surface, showing the appearance of characteristic DNA peaks after aptamer immobilization.

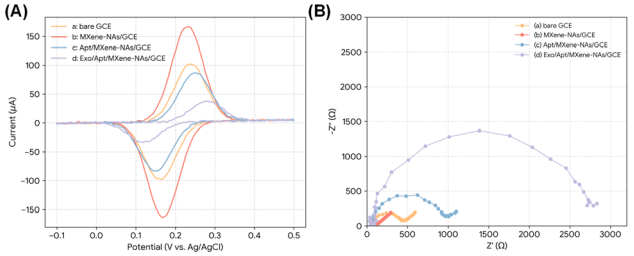

Fig. 8 Electrochemical characterization of step-type inductance sensor preparation. (A) Cyclic voltammeter diagram and (B) EIS Nyquist plots of bare GCE, MXene–NAs/GCE, Apt/MXene–NAs/GCE and Exo/Apt/MXene–NAs/GCE's int 5.0 mM $[Fe(CN)_6]^{3-/4-}$ containing 0.1 M KCl.

In addition, aptamer immobilization was first supported by FTIR spectroscopy (Fig. 7B). After incubation with the thiolated CD63 aptamer, new bands appeared at approximately 1654, 1240, and 1080 cm^{-1}, assignable to nucleobase-associated vibrations and phosphate stretching modes of the DNA backbone. This interpretation is further supported by the ζ-potential shift observed for the dispersion-phase analogue after aptamer treatment. Because FTIR and ζ-potential are not fully quantitative descriptors of surface loading, we further examined the aptamer-functionalized interface by XPS. Compared with MXene–NAs, the Apt/MXene–NAs surface exhibited the appearance of a P 2p signal centered at ~133 eV, attributable to phosphate groups from the immobilized DNA aptamer, together with an increased N 1s contribution, providing stronger chemical evidence for successful aptamer immobilization on the Au-containing nanoalloy interface.

3.2 Electrochemical characterization during aptasensor fabrication

The sequential construction of the aptamer sensor was tracked by cyclic voltammetry (CV) and electrochemical impedance spectroscopy (EIS), both of which are effective methods for evaluating the changes at the electrodel-solution interface. As shown in Fig. 8A, the CV reaction was recorded in 5.0 mM $[Fe(CN)_6]^{3-/4-}$ solution. The exposed GCE (curve *a*) shows a pair of distinct REDOX peaks, with a separation between peaks of 78 mV, indicating quasi-reversible electron transfer. After coating with MXene–NAs nanocomposites (curve *b*), the peak REDOX current increased significantly, and ΔE decreased to 62 mV. This improvement stems from the high electrical conductivity and large active surface area of MXene–NAs, which promotes the electron exchange between the REDOX probe and the electrode surface.[53,54]

After fixing the CD63 adapting (curve *c*), the peak current decreases and the ΔE_p increases. This behavior can be explained by the negatively charged phosphate skeleton of the DNA adaptive body, which can repel $[Fe(CN)_6]^{3-/4-}$, and the biomolecular layer itself partially prevents electron transfer. After the subsequent CRC exosome binding (curve *d*), this blocking effect was further enhanced.[55] Because the exosome body is a relatively large vesicle, their capture on the electrode surface forms an insulating layer, which strongly restricts the entry of the redox probe, resulting in a significant reduction in current response.[56] This improvement stems from the high electrical conductivity and the increased electrochemically accessible surface created by the nanostructured MXene–AuPtPdCu coating. To quantify the active-area change during stepwise fabrication, we estimated the electrochemically active surface area (ECSA) from scan-rate-dependent CVs of a reversible redox probe using the Randles–Ševčík relationship ($i_p \propto A \cdot \nu^{1/2}$). Under identical electrolyte/probe conditions, the calculated ECSA increased from 0.073 cm^2 for bare GCE to 0.156 cm^2 after MXene–NAs modification (≈2.14-fold), confirming that the composite coating exposes additional accessible electroactive sites. After aptamer immobilization, the ECSA decreased to 0.140 cm^2, and further decreased to 0.108 cm^2 after exosome capture, consistent with progressive surface blocking by the negatively charged aptamer layer and the insulating vesicle adlayer that limits probe access and electron transfer.

The CV results are consistent with the EIS analysis results, and they are highly sensitive to changes in interface resistance. The Nyquist diagram in Fig. 8B shows the hypothetical impedance ($-Z'$) and the actual impedance (Z'), in which the diameter of the high-frequency semicircle reflects the charge transfer resistance (R_{ct}). The exposed GCE (curve *a*) shows a small semicircle, corresponding to 350 Ω R_{ct}. After being modified by MXene–NAs, the figure is close to the vertical line, and the R_{ct} is greatly reduced to 45 Ω, confirming that the nanocomposite layer has excellent electrical conductivity. On the contrary, due to the insulating properties of the DNA layer, the adhesion of the adaptive body leads to a sharp increase in R_{ct} to 850 Ω. After the exosome is captured, R_{ct} reaches a maximum value of 2600 Ω, indicating that the binding event constitutes a substantial obstacle to charge transfer.[32] Table 2 summarizes the fitted EIS parameters during stepwise assembly, including the charge-transfer resistance R_{ct} and the constant-phase-element parameters (Q, n) used to describe the non-ideal double layer. In addition to the marked increase in R_{ct} after aptamer immobilization and exosome capture, the fitted CPE/effective C_{dl} values also changed systematically, indicating alteration of the interfacial double layer caused by biomolecular adsorption and surface blocking. Collectively, the progressive faradaic suppression in CV/DPV and the marked increase in R_{ct} after aptamer immobilization and exosome capture indicate the formation of an increasingly blocking interfacial adlayer that limits redox-probe access and slows interfacial electron transfer. We note that for the anionic $[Fe(CN)_6]^{3-/4-}$ probe, the

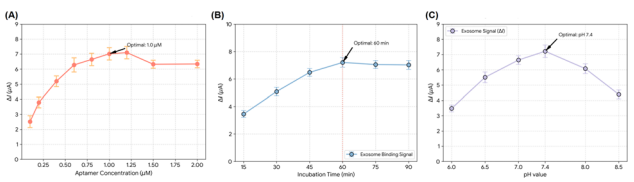

Fig. 9 Optimization of aptasensor conditions: effects of (A) aptamer concentration, (B) incubation time, (C) buffer pH on the DPV signal change (Δ*I*) during detection of 1 × 10^3 particles per μL CRC exosomes.

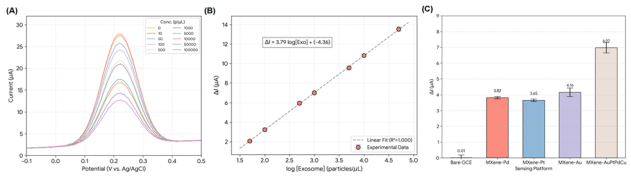

Fig. 10 (A) In 5.0 mM $[Fe(CN)_6]^{3-/4-}$ containing 0.1 M KCl, as the concentration of CRC exosomes increased (from top to bottom). The DPV response recorded by the aptamer sensor after incubation at 0, 10, 50, 100, 500, 1×10^3, 5×10^3, 1×10^4, 5×10^4 and 1×10^5 particles per microliter. (B) The corresponding calibration curve for the quantitative detection of CRC exosomes. This figure shows the dependence of DPV signal changes (ΔI) on the logarithm of exosome concentration, and the error line represents the standard deviation of three independent measurements. (C) Comparison of DPV signal changes (ΔI) when 1×10^3 particles per microliter CRC exosomes were detected using aptor sensors based on GCE, MXene–Pd, MXene–Pt, MXene–Au and the proposed MXene–AuPtPdCu platform.

observed signal decrease can arise from a combination of steric exclusion and electrostatic effects, and EIS is, in principle, sensitive to both resistive and capacitive interfacial changes upon biomolecule adsorption.

This charge-based effect is further supported by ζ-potential measurements performed on a dispersion-phase analogue of the surface functionalization, where aptamer treatment shifted the ζ-potential of MXene–NAs from -21.0 ± 1.8 mV to -27.6 ± 1.5 mV, consistent with incorporation of the negatively charged phosphate backbone. We now clarify in the revised manuscript that this result should be viewed as supportive rather than quantitative, and we therefore include XPS-based evidence of the DNA phosphate signal as a stronger orthogonal confirmation of aptamer immobilization.

3.3 Optimization of experimental conditions

In order to obtain the best analytical performance, the key experimental factors are systematically optimized. These include the concentration of immobilized aptamer, the incubation time of exosome capture and the pH of the buffer measured. Take the peak current change (ΔI) of DPV as the optimization index. As shown in Fig. 9A, as the concentration of the suitable body increases from 0.1 μM to 1.0 μM, the ΔI response increases. This trend shows that the high surface coverage of the lind can capture more exosome, which leads to greater signal changes. However, when the concentration is higher than 1.0 μM, the ΔI value tends to stabilize and then decreases slightly, which may be due to the presence of spatial resistance between densely arranged body molecules, thus reducing their binding efficiency. Therefore, the optimal value is the optimal concentration of 1.0 μM. Then evaluate the impact of incubation time in the range of 15 to 90 minutes (Fig. 9B). The ΔI response gradually increases with the extension of the incubation time and reaches a stable level at about 60 minutes, indicating that the interaction between the aditable body and the exosome body is close to equilibrium. According to this result, an incubation period of 60 minutes is used for follow-up measurement. In addition, the effect of solution pH on DPV response was examined between pH 6.0 and 8.5 (Fig. 9C). At pH 7.4, the ΔI value is the highest, which is close to physiological conditions, which is conducive to preserving the structure of the body and the stability of the exosome. Therefore, PBS with a pH of 7.4 should be selected as the best supporting electrolyte for further experiments.

3.4 Analytical performance of the aptasensor

Under optimized experimental conditions, the DPV method is used to evaluate the quantitative performance of the CRC exosome detection adaptive sensor based on MXene–NAs. It can be seen from Fig. 10A that in the concentration range of 10–1×10^5 particles per μL, the DPV signal after exposure to CRC exosome, the peak current decreases systematically with the increase in the number of exosome. This trend is consistent with an interfacial blocking mechanism: increasing exosome concentration leads to more binding events on the electrode surface, producing a denser insulating/biomolecular adlayer that reduces effective probe accessibility and increases the electron-transfer barrier, thereby decreasing the DPV current. Given the anionic nature of $[Fe(CN)_6]^{3-/4-}$ and the negatively charged aptamer/exosome interface, electrostatic repulsion may contribute in parallel to the observed suppression.[57]

The corresponding calibration curve is shown in Fig. 10B, showing the DPV peak current change (ΔI) as a function of the exosome concentration logarithm. A good linear relationship was found in the range of 50 to 5×10^4 particles per μL. The linear regression equation is ΔI (μA) = 3.85 log[exo] (particle per μL) – 4.52, and the correlation coefficient (R^2) is 0.998. The LOD was calculated using the $3\sigma/S$ criterion, where S is the slope of the calibration curve and σ is the standard deviation of repeated blank responses (ΔI) recorded in the absence of exosomes. Here, the blank was defined as the DPV response obtained after incubating the prepared Apt/MXene–NAs/GCE in exosome-free PBS (pH 7.4) under the same conditions used for analysis (37 °C, 60 min), followed by DPV measurement in 5.0 mM $[Fe(CN)_6]^{3-/4-}$ containing 0.1 M KCl. The blank was measured using multiple independently prepared electrodes and/or repeated runs ($n \geq 10$), and σ was taken as the standard deviation of these blank ΔI values. Based on these blank measurements in buffer, the analytical LOD was 19 particles per μL. Because matrix constituents can increase blank variability and thereby inflate σ, we additionally define a matrix blank using 10-fold diluted, exosome-depleted human serum processed identically, and we report the corresponding matrix-based LOD ($3\sigma_{matrix}/S$) as a practical estimate for real samples. The detection limit is very low, which proves the high sensitivity of the proposed sensor. Table 3 compares the performance of our adaptor sensor with other recently reported exosome detection methods.

The corresponding calibration relationship is shown in Fig. 10B, in which the DPV peak current change (ΔI) is drawn according to the logarithm of the exosome concentration. A clear linear dependence was obtained in the concentration range of 50 to 5×10^4 particles per μL. The regression formula ΔI (μA) = 3.85 log[exo]particles per μL – 4.52 is obtained by

linear fitting, and the correlation coefficient (R^2) is 0.998, which is very linear. The detection limit LOD is determined by the $3\sigma/S$ method. S is the slope of the calibration curve, and σ is the standard deviation of the blank signal when the detection level is 19 particles per μL. The low detection limit also reflects the good sensitivity of the sensor. Table 3 shows the performance comparison of this sensor with other recently published exosome detection strategies. The results show that our sensor has a low or equivalent LOD and a wide linear range, highlighting its competitive advantage in clinical applications.[11,59]

To highlight the critical role of the AuPtPdCu high-entropy nanoalloy, the performance of the fully constructed aptasensor was compared with control sensors fabricated with monometallic (MXene–Au, MXene–Pt, MXene–Pd) and unmodified GCE platforms (Fig. 10C). Under the same conditions for detecting 1×10^3 particles per μL of exosomes, the aptasensor based on MXene–AuPtPdCu exhibited a ΔI of 7.02 μA. In contrast, the signals change from the sensors made of MXene–Au, MXene–Pt, and MXene–Pd are much smaller: 4.15 μA, 3.58 μA, and 3.81 μA, respectively. The bare GCE modified with the aptamer showed a negligible response. This result unequivocally demonstrates the superior performance of the high-entropy nanoalloy, which can be attributed to the synergistic electrocatalytic effects and enhanced conductivity arising from the multi-component alloy structure, leading to significant signal amplification.

CRC exosomes used for analytical calibration were isolated from colorectal cancer cell-culture supernatants, while vesicles used for clinical analysis were obtained from human serum samples. Briefly, samples were subjected to sequential low-speed centrifugation to remove cells and debris, followed by exosome enrichment using ultracentrifugation (or the authors' actual kit/method, if different). The final pellet was resuspended in sterile PBS and stored at −80 °C until use. Particle concentration and size distribution were determined by nanoparticle tracking analysis (NTA), which showed a predominant vesicle population within the expected exosome size range. Vesicle morphology was confirmed by transmission electron microscopy, and the exosomal identity was verified by marker proteins such as CD63/CD81/TSG101 (with an appropriate negative marker such as calnexin, if available).[62] Exosome concentrations used in the electrochemical assay were expressed as particles per μL based on NTA results.

3.5 Selectivity, reproducibility, and stability

Selectivity is a key requirement for applying the aptasensor in complex biological matrices. The sensor response to CRC-derived exosomes (CRC-Exo, 1×10^3 particles per μL) was compared with several potential interferents at higher challenge levels, including bovine serum albumin (BSA, 100 μg mL^{-1}), exosomes from healthy fibroblast cells (HF-Exo, 1×10^4 particles per μL), and exosomes from a breast cancer cell line (MCF7-Exo, 1×10^4 particles per μL). Notably, the particle concentrations here were normalized by total particle counting; because EV populations are heterogeneous, the fraction of CD63-presenting vesicles and the surface-accessible CD63

Table 3 Comparison of the proposed aptasensor with previously reported exosome sensors

Sensing platform	Detection method	Linear range (particles per mL)	LOD (particles per mL)	Assay time per measurement	Operational complexity	Sample volume	Reproducibility/ realistic-matrix performance	Reference
MXene–AuPtPdCu aptameric electrode	DPV	5.0×10^4–5.0×10^7	1.9×10^4	~60 min incubation + <5 min DPV readout	Moderate (single capture step, label-free electrochemical readout)	200 μL	Inter-electrode RSD 4.5%; intra-assay RSD 3.2%; serum spike recovery 96.8–104.2% (RSD < 5.0%)	This work
AuPt NCs/Ti_3C_2-MXene	ECL	1.0×10^5–5.0×10^8	2.0×10^4	NR	High (ECL labeling and optical instrumentation)	NR	NR	58
AuNP-based biosensor	SPR	1.1×10^8–1.1×10^{11}	9.6×10^4	NR	Moderate–High (chip functionalization and SPR system)	NR	Tested in diluted serum; detailed RSD NR	59
Magnetic beads/AuNPs	Colorimetric	2.5×10^6–1.0×10^{10}	1.6×10^5	NR	High (magnetic separation and multistep labeling)	NR	NR	60
nPLEX nanoplasmonic chip	Nanoplasmonic	6.7×10^5–1.0×10^{12}	3.0×10^6	NR	Moderate (microfabricated chip with optical readout)	NR	NR	61

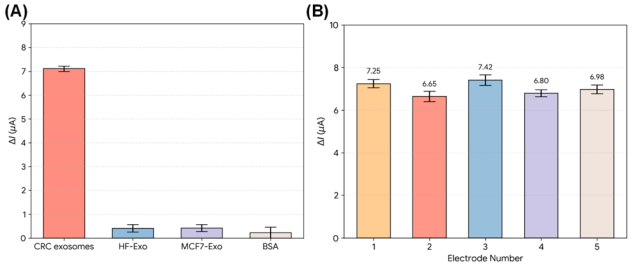

Fig. 11 (A) Selectivity of the aptasensor. DPV signal change in response to target CRC exosomes (1×10^3 particles per μL) and potential interfering substances: BSA (100 μg mL^{-1}), healthy fibroblast exosomes (HF-Exo, 1×10^4 particles per μL), and breast cancer exosomes (MCF7-Exo, 1×10^4 particles per μL). (B) Reproducibility of the aptasensor. DPV responses for the detection of 1×10^3 particles per μL exosomes using five independently fabricated electrodes. (C) Long-term stability of the aptasensor. The sensor was stored at 4 °C and its DPV response to 1×10^3 particles per μL exosomes was measured periodically over 28 days.

density can differ substantially across cell lines and isolation conditions, so equal total particle numbers do not necessarily correspond to equal CD63 binding-site availability. Consistent with this principle, Fig. 11A shows that CRC-Exo generates a pronounced ΔI decrease, whereas HF-Exo and MCF7-Exo produce only minor signal changes even at 10-fold higher total particle concentration. This behavior indicates that our interface effectively captures vesicles with sufficiently exposed CD63 to form an insulating layer and block $[Fe(CN)_6]^{3-/4-}$ transport. The discrimination observed in this selectivity panel therefore reflects practical differences in CD63 presentation/capture efficiency among the tested samples rather than any tumor-type 'specificity' of CD63 itself. The repeatability and stability of the sensor were further tested. Under the condition of 1×10^3 particles per microliter, five intra-batch measurements were conducted using a single aptamer sensor, and the relative standard deviation obtained was 3.2%. Inter-assay reproducibility, evaluated using five independently prepared sensors, showed an RSD of 4.5% (Fig. 11B), indicating good fabrication consistency. For stability assessment, aptasensors stored at 4 °C maintained 94.6% of their initial DPV response after 28 days (Fig. 11C), demonstrating satisfactory long-term stability.[11]

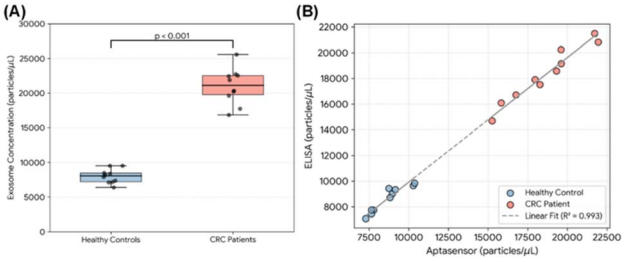

Fig. 12 Clinical sample analysis. (A) The box diagram shows the serum exosome level measured by the adaptive sensor of CRC patients (n = 10) and healthy control group (n = 10). (B) Correlation between measurements obtained with the proposed DPV aptasensor and a commercial ELISA kit.

Table 4 Determination of CRC exosomes in spiked human serum samples (n = 3)

Sample	Spiked (particles per μL)	Found (particles per μL)	Recovery (%)	RSD (%)
1	100	96.8	96.8	4.8
2	1000	1042.1	104.2	3.5
3	10 000	9855.7	98.6	4.1

3.6 Analysis of clinical samples

The aptasensor was tested on serum from 10 CRC patients and 10 healthy controls, with results benchmarked against a commercial CD63 ELISA kit to assess clinical applicability. As shown in Fig. 12A, the exosome concentrations measured by our aptasensor were significantly higher in the CRC patient group (average of 2.1×10^4 particles per μL) compared to the healthy control group (average of 0.8×10^4 particles per μL), with a p-value < 0.001. This result indicates that the sensor can effectively distinguish between CRC patients and healthy individuals. DPV results from the aptasensor show a linear correlation with ELISA (R^2 = 0.995; Fig. 12B), confirming accuracy and reliability. Recovery tests in 10-fold diluted healthy serum spiked with CRC exosomes yielded 96.8–104.2% recovery with RSDs <5.0% (Table 4), demonstrating robustness against matrix effects and reliable serum quantification. This pilot clinical comparison supports the ability of the sensor to separate CRC and healthy sera under controlled conditions, but it is not intended to establish definitive clinical performance.

The current clinical assessment is limited by the small single-center sample size (n = 10 per group) and the absence of stage stratification. We did not perform an *a priori* power analysis for this pilot feasibility set; instead, we use effect sizes and confidence intervals to summarize the observed separation and to inform future study design, noting that post hoc power based on observed effects is not a reliable substitute for prospective planning. In future work, we will conduct a prospective, multi-center validation enrolling CRC patients across stages (I–IV) together with appropriate controls, using standardized pre-analytical handling and blinded testing, with a pre-specified sample-size calculation targeting adequate precision for estimated accuracy metrics (*e.g.*, AUC/sensitivity/specificity confidence intervals) and/or stage-wise comparisons, consistent with reporting guidance for diagnostic/biomarker studies.

4. Conclusion

In short, researchers have developed a highly sensitive electrochemically adapted sensor for quantitatively detecting exosome bodies originating from colorectal cancer. $Ti_3C_2T_x$ MXene. The obtained MXene–nanoalloy composite has high conductivity and large active surface area, and the synergy effect of polymetallic nanoalloy significantly enhances the electrochemical response. Based on the specific identification of the surface protein CD63 of the exosome body, the adaptive sensor showed excellent analytical performance in differential pulse

voltammetric detection. The lower limit of the detection was as low as 19 particles per microliter, and the linear range was 50 to 5×10^4 particles per microliter. The sensor also exhibited high selectivity, good reproducibility (RSD < 4.5%), and strong stability, maintaining more than 94% of its initial response after 28 days. Importantly, successful analysis of human serum samples demonstrated clear discrimination between CRC patients and healthy individuals, with results closely matching those from ELISA assays. Overall, this MXene–NAs-based aptasensor provides a sensitive, reliable, and simple approach for liquid biopsy and shows strong potential for early, noninvasive CRC diagnosis and monitoring, while offering a versatile strategy for future biosensor design using MXene and high-entropy nanoalloy composites.

Ethical statement

All experiments were performed in accordance with the Guidelines of the Declaration of Helsinki, and experiments were approved by the ethics committee at Suzhou TCM Hospital Affiliated to Nanjing University of Chinese Medicine. Informed consents were obtained from human participants of this study.

Author contributions

YY and SY conceptualized the study and designed the experimental framework. YY and TC performed the experiments and carried out data collection. MY contributed to nanomaterial synthesis and structural characterization. HF assisted with clinical sample collection and validation experiments. LS conducted formal analysis and statistical evaluation. MS supervised the project, contributed to methodology refinement, and secured funding acquisition. YY drafted the original manuscript. SY and MS critically reviewed and edited the manuscript. All authors have read and agreed to the published version of the manuscript.

Conflicts of interest

There are no conflicts to declare.

Data availability

All the data generated during and/or analyzed during the current study are available from the corresponding author upon reasonable request.

Supplementary information (SI) is available. See DOI: https://doi.org/10.1039/d6ra01343k.

Acknowledgements

This work was financially supported by the Development Plan of Traditional Chinese Medicine Science and Technology in Jiangsu Province (Grants No. MS2025069), the Natural Science Foundation of Jiangsu Province (Grants No. BK20240385), Suzhou Medical and Health Science and Technology Innovation Project (Grants No. SKY2023216), Gusu Health Talent Program (GSWS2024085), Natural Science Foundation of Nanjing University of Chinese Medicine (Grants No. XZR2024064) and Suzhou Science and Education Promoting Health Project (Grants No. MSXM2024025).

References

1 T. Zhang, Y. Guo, B. Qiu, X. Dai, Y. Wang and X. Cao, *Front. Oncol.*, 2024, **14**, 1466159.
2 T. Matsuda, A. Fujimoto and Y. Igarashi, *Digestion*, 2025, **106**, 91–99.
3 S. Madar, R. E. Amor, S. Furman-Assaf and E. Friedman, *Cancers*, 2025, **17**, 1867.
4 N. Chacko and R. Ankri, *Clin. Exp. Med.*, 2025, **25**, 17.
5 Y. Yao, Z. Huang, P. Xie, S. D. Lacey, R. J. Jacob, H. Xie, F. Chen, A. Nie, T. Pu, M. Rehwoldt, D. Yu, M. R. Zachariah, C. Wang, R. Shahbazian-Yassar, J. Li and L. Hu, *Science*, 2018, **359**, 1489–1494.
6 M. I. Mosquera-Heredia, L. C. Morales, O. M. Vidal, E. Barceló, C. Silvera-Redondo, J. I. Vélez and P. Garavito-Galofre, *Biomedicines*, 2021, **9**, 1061.
7 K. K. Jella, T. H. Nasti, Z. Li, S. R. Malla, Z. S. Buchwald and M. K. Khan, *Vaccines*, 2018, **6**, 69.
8 D.-S. Sun and H.-H. Chang, *Tzu Chi Med. J.*, 2024, **36**, 251–259.
9 B. Alkan, L. Duarte-Correa, F. Girgsdies, G. Koch, J. Kröhnert, M. Ertegi, S. Jiang, T. Lunkenbein and A. Trunschke, *ACS Catal.*, 2025, **15**, 5781–5795.
10 Q. Zhou, A. Rahimian, K. Son, D.-S. Shin, T. Patel and A. Revzin, *Methods*, 2016, **97**, 88–93.
11 W. Feng, P. Xu, M. Wang, G. Wang, G. Li and A. Jing, *Micromachines*, 2023, **14**, 138.
12 L.-F. Kuang, L. Zhang, H. Li, H.-Y. Qin, H.-Z. Chi, J.-B. Liu, J. Zhang, F. Yan and X.-Z. Xiao, *cMat*, 2024, **1**, e26.
13 G. Zhang, S. Cen, X. Huang, X. Yu, H. Zhu, L. Sun, R. Su, C. Yang and Z. Zhu, *Anal. Chem.*, 2024, **96**, 17897–17906.
14 N. N. Alias, A. Masood, P. C. Ooi, M. Ahmadipour, M. A. Mohamed, A. M. Hashim, A. Ali Umar and M. A. S. Mohammad Haniff, *ACS Appl. Bio Mater.*, 2025, **8**, 9557–9588.
15 M. Ahmadipour, A. Bhattacharya, M. Sarafbidabad, E. Syuhada Sazali, S. Krishna Ghoshal, M. Satgunam, R. Singh, M. Rezaei Ardani, N. Missaoui, H. Kahri, U. Pal and A. Ling Pang, *Clin. Chim. Acta*, 2024, **554**, 117788.
16 M. Balyan, M. Ahmadipour, Z. A. Ahmad and B. Siregar, *Appl. Phys. A*, 2024, **130**, 638.
17 A. Barhoum, S. Hamimed, H. Slimi, A. Othmani, F. M. Abdel-Haleem and M. Bechelany, *Trends Environ. Anal. Chem.*, 2023, **38**, e00199.
18 M. Rostami, A. Badiei and G. M. Ziarani, *Inorg. Chem. Commun.*, 2024, **163**, 112362.
19 Q. Wang, N. Han, Z. Shen, X. Li, Z. Chen, Y. Cao, W. Si, F. Wang, B.-J. Ni and V. K. Thakur, *Nano Mater. Sci.*, 2023, **5**, 39–52.
20 M. Naguib, M. Kurtoglu, V. Presser, J. Lu, J. Niu, M. Heon, L. Hultman, Y. Gogotsi and M. W. Barsoum, *Adv. Mater.*, 2011, **23**, 4248–4253.

21 M. Ghidiu, M. R. Lukatskaya, M.-Q. Zhao, Y. G. Gogotsi and M. W. Barsoum, *Nature*, 2014, **516**, 78–81.
22 W. Cao, J. Nie, Y. Cao, C. Gao, M. Wang, W. Wang, X. Lu, X. Ma and P. Zhong, *Chem. Eng. J.*, 2024, **496**, 154097.
23 T. Habib, X. Zhao, S. A. Shah, Y. Chen, W. Sun, H. An, J. L. Lutkenhaus, M. Radovic and M. J. Green, *npj 2D Mater. Appl.*, 2019, **3**, 8.
24 W. Putzbach and N. J. Ronkainen, *Sensors*, 2013, **13**, 4811–4840.
25 J. Chen, A. Wu, Y. Zhang, Y. Xie, H. Zheng and W. Teng, *Front. Mater.*, 2025, **12**, 1613997.
26 E. J. Pickering and N. G. Jones, *Int. Mater. Rev.*, 2016, **61**, 183–202.
27 A. B. Steel, T. M. Herne and M. J. Tarlov, *Anal. Chem.*, 1998, **70**, 4670–4677.
28 T. M. Herne and M. J. Tarlov, *J. Am. Chem. Soc.*, 1997, **119**, 8916–8920.
29 Z.-P. Wu, D. T. Caracciolo, Y. Maswadeh, J. Wen, Z. Kong, S. Shan, J. A. Vargas, S. Yan, E. Hopkins, K. Park, A. Sharma, Y. Ren, V. Petkov, L. Wang and C.-J. Zhong, *Nat. Commun.*, 2021, **12**, 859.
30 L. Sun, K. Wen, G. Li, X. Zhang, X. Zeng, B. Johannessen and S. Zhang, *ACS Mater. Au*, 2024, **4**, 547–556.
31 D. Jiang, X. Cao, Y. Shi, J. Chen, X. Li, J. Liu and H. Zhou, *Adv. Funct. Mater.*, 2024, **34**, 2410546.
32 J. Gao, R. Yang, X. Zhu, J. Shi, S. Wang and A. Jing, *Micromachines*, 2025, **16**, 280.
33 B. Jiang, T. Zhang, S. Liu, Y. Sheng and J. Hu, *J. Nanobiotechnol.*, 2024, **22**, 55.
34 S. Wu, Y. Liu, Y. Ren, Q. Wei and Y. Sun, *Nano Res.*, 2022, **15**, 4886–4892.
35 A. Y. El-Moghazy, N. Amaly, N. Nitin and G. Sun, *Lab Chip*, 2023, **23**, 5009–5017.
36 V. Liustrovaite, D. Karoblis, B. Brasiunas, A. Popov, A. Katelnikovas, A. Kareiva, A. Ramanavicius, R. Viter, M. T. Giardi, D. Erts and A. Ramanaviciene, *Int. J. Mol. Sci.*, 2023, **24**, 5803.
37 T. Laochai, J. Yukird, N. Promphet, J. Qin, O. Chailapakul and N. Rodthongkum, *Biosens. Bioelectron.*, 2022, **203**, 114039.
38 K. M. Chahrour, P. C. Ooi, A. A. Nazeer, L. A. Al-Hajji, P. R. Jubu, C. F. Dee, M. Ahmadipour and A. A. Hamzah, *New J. Chem.*, 2023, **47**, 7890–7902.
39 M. Ahmadipour, A. L. Pang, M. R. Ardani, S.-Y. Pung, P. C. Ooi, A. A. Hamzah, M. F. Mohd Razip Wee, M. Aniq Shazni Mohammad Haniff, C. F. Dee, E. Mahmoudi, A. Arsad, M. Z. Ahmad, U. Pal, K. M. Chahrour and S. A. Haddadi, *Mater. Sci. Semicond. Process.*, 2022, **149**, 106897.
40 M. Ahmadipour, M. Ahmadipour, U. Pal and M. Satgunam, *Microchem. J.*, 2025, **216**, 114765.
41 H. K. Jazi, M. Sarafbidabad, M. B. Henda and M. Ahmadipour, *Diamond Relat. Mater.*, 2025, **151**, 111845.
42 W. Lei, M. Sun, W. Zhang, L. Liang, Z. Ding, X. Tang, H. Dai, X. Liu, P. Qi and Y. Wang, *Chem. Eng. J.*, 2026, **530**, 173410.
43 Y. Feng, Z. Ding, S. Tang, X. Liu, P. Qi and Y. Wang, *Chem. Eng. J.*, 2025, **522**, 167505.
44 K. S. Kim, M. Couillard, Z. Tang, H. Shin, D. Poitras, C. Cheng, O. Naboka, D. Ruth, M. Plunkett, L. Chen, L. Gaburici, T. Lacelle, M. Nganbe and Y. Zou, *Nat. Commun.*, 2024, **15**, 1450.
45 L. S. R. Kumara, O. Sakata, H. Kobayashi, C. Song, S. Kohara, T. Ina, T. Yoshimoto, S. Yoshioka, S. Matsumura and H. Kitagawa, *Sci. Rep.*, 2017, **7**, 14606.
46 J. Halim, K. M. Cook, M. Naguib, P. Eklund, Y. Gogotsi and J. Rosen, *Appl. Surf. Sci.*, 2016, **362**, 406–417.
47 C. Yin, J. B. Miller, P. Kondratyuk and A. J. Gellman, *J. Phys. Chem. B*, 2018, **122**, 764–769.
48 Y. Yao, Z. Huang, P. Xie, S. D. Lacey, R. J. Jacob, H. Xie, F. Chen, A. Nie, T. Pu, M. Rehwoldt, D. Yu, M. R. Zachariah, C. Wang, R. Shahbazian-Yassar, J. Li and L. Hu, *Science*, 2018, **359**, 1489–1494.
49 Y. Lu, D. Li and F. Liu, *Materials*, 2022, **15**, 307.
50 H. Lu, Z. Kong, Y. Yang, Z. Xie, H. Xiang, S. Liu and G. Yu, *Electrocatalysis*, 2021, **12**, 372–380.
51 V. A. Tran, T. T. V. Tran, V. T. Le, V. D. Doan, G. N. L. Vo, V. H. Tran, H. Jeong and T. T. T. Vo, *Appl. Mater. Today*, 2024, **38**, 102217.
52 Z. Huang, J. Peng, L. Xu and P. Liu, *Nanomaterials*, 2024, **14**, 1417.
53 V. Natu, M. Benchakar, C. Canaff, A. Habrioux, S. Célérier and M. W. Barsoum, *Matter*, 2021, **4**, 1224–1251.
54 H. Zhang, Z. Wang, Q. Zhang, F. Wang and Y. Liu, *Biosens. Bioelectron.*, 2019, **124–125**, 184–190.
55 W. Wang, S. Qiao, X. Kong, G. Zhang and Z. Cai, *Cell. Mol. Immunol.*, 2025, **22**, 975–995.
56 I. Kimiz-Gebologlu and S. S. Oncel, *J. Controlled Release*, 2022, **347**, 533–543.
57 K. J. Aoki, J. Chen, Y. Liu and B. Jia, *J. Electroanal. Chem.*, 2020, **856**, 113609.
58 H. Zhang, Z. Wang, F. Wang, Y. Zhang, H. Wang and Y. Liu, *Anal. Chem.*, 2020, **92**, 5546–5553.
59 Q. Wang, L. Zou, X. Yang, X. Liu, W. Nie, Y. Zheng, Q. Cheng and K. Wang, *Biosens. Bioelectron.*, 2019, **135**, 129–136.
60 B. Martín-Gracia, A. Martín-Barreiro, C. Cuestas-Ayllón, V. Grazú, A. Line, A. Llorente, J. M. de la Fuente and M. Moros, *J. Mater. Chem. B*, 2020, **8**, 6710–6738.
61 A.-E. Radi and M. R. Abd-Ellatief, *Diagnostics*, 2021, **11**, 104.
62 C. Théry, K. W. Witwer, E. Aikawa, M. J. Alcaraz, J. D. Anderson, R. Andriantsitohaina, A. Antoniou, T. Arab, F. Archer, G. K. Atkin-Smith, D. C. Ayre, J. Bach, D. Bachurski, H. Baharvand, L. Balaj, S. Baldacchino, N. N. Bauer, A. A. Baxter, M. Bebawy, C. Beckham, A. Bedina Zavec, A. Benmoussa, A. C. Berardi, P. Bergese, E. Bielska, C. Blenkiron, S. Bobis-Wozowicz, E. Boilard, W. Boireau, A. Bongiovanni, F. E. Borràs, S. Bosch, C. M. Boulanger, X. Breakefield, A. M. Breglio, M. Á. Brennan, D. R. Brigstock, A. Brisson, M. L. Broekman, J. F. Bromberg, P. Bryl-Górecka, S. Buch, A. H. Buck, D. Burger, S. Busatto, D. Buschmann, B. Bussolati, E. I. Buzás, J. B. Byrd, G. Camussi, D. R. Carter, S. Caruso, L. W. Chamley, Y. Chang, C. Chen, S. Chen, L. Cheng, A. R. Chin, A. Clayton, S. P. Clerici, A. Cocks, E. Cocucci, R. J. Coffey, A. Cordeiro-da-Silva,

Y. Couch, F. A. Coumans, B. Coyle, R. Crescitelli, M. F. Criado, C. D'Souza-Schorey, S. Das, A. Datta Chaudhuri, P. De Candia, E. F. De Santana, O. De Wever, H. A. Del Portillo, T. Demaret, S. Deville, A. Devitt, B. Dhondt, D. Di Vizio, L. C. Dieterich, V. Dolo, A. P. Dominguez Rubio, M. Dominici, M. R. Dourado, T. A. Driedonks, F. V. Duarte, H. M. Duncan, R. M. Eichenberger, K. Ekström, S. El Andaloussi, C. Elie-Caille, U. Erdbrügger, J. M. Falcón-Pérez, F. Fatima, J. E. Fish, M. Flores-Bellver, A. Försönits, A. Frelet-Barrand, F. Fricke, G. Fuhrmann, S. Gabrielsson, A. Gámez-Valero, C. Gardiner, K. Gärtner, R. Gaudin, Y. S. Gho, B. Giebel, C. Gilbert, M. Gimona, I. Giusti, D. C. Goberdhan, A. Görgens, S. M. Gorski, D. W. Greening, J. C. Gross, A. Gualerzi, G. N. Gupta, D. Gustafson, A. Handberg, R. A. Haraszti, P. Harrison, H. Hegyesi, A. Hendrix, A. F. Hill, F. H. Hochberg, K. F. Hoffmann, B. Holder, H. Holthofer, B. Hosseinkhani, G. Hu, Y. Huang, V. Huber, S. Hunt, A. G. Ibrahim, T. Ikezu, J. M. Inal, M. Isin, A. Ivanova, H. K. Jackson, S. Jacobsen, S. M. Jay, M. Jayachandran, G. Jenster, L. Jiang, S. M. Johnson, J. C. Jones, A. Jong, T. Jovanovic-Talisman, S. Jung, R. Kalluri, S. Kano, S. Kaur, Y. Kawamura, E. T. Keller, D. Khamari, E. Khomyakova, A. Khvorova, P. Kierulf, K. P. Kim, T. Kislinger, M. Klingeborn, D. J. Klinke, M. Kornek, M. M. Kosanović, Á. F. Kovács, E. Krämer-Albers, S. Krasemann, M. Krause, I. V. Kurochkin, G. D. Kusuma, S. Kuypers, S. Laitinen, S. M. Langevin, L. R. Languino, J. Lannigan, C. Lässer, L. C. Laurent, G. Lavieu, E. Lázaro-Ibáñez, S. Le Lay, M. Lee, Y. X. F. Lee, D. S. Lemos, M. Lenassi, A. Leszczynska, I. T. Li, K. Liao, S. F. Libregts, E. Ligeti, R. Lim, S. K. Lim, A. Linē, K. Linnemannstöns, A. Llorente, C. A. Lombard, M. J. Lorenowicz, Á. M. Lörincz, J. Lötvall, J. Lovett, M. C. Lowry, X. Loyer, Q. Lu, B. Lukomska, T. R. Lunavat, S. L. Maas, H. Malhi, A. Marcilla, J. Mariani, J. Mariscal, E. S. Martens-Uzunova, L. Martin-Jaular, M. C. Martinez, V. R. Martins, M. Mathieu, S. Mathivanan, M. Maugeri, L. K. McGinnis, M. J. McVey, D. G. Meckes, K. L. Meehan, I. Mertens, V. R. Minciacchi, A. Möller, M. Møller Jørgensen, A. Morales-Kastresana, J. Morhayim, F. Mullier, M. Muraca, L. Musante, V. Mussack, D. C. Muth, K. H. Myburgh, T. Najrana, M. Nawaz, I. Nazarenko, P. Nejsum, C. Neri, T. Neri, R. Nieuwland, L. Nimrichter, J. P. Nolan, E. N. Nolte-'t Hoen, N. Noren Hooten, L. O'Driscoll, T. O'Grady, A. O'Loghlen, T. Ochiya, M. Olivier, A. Ortiz, L. A. Ortiz, X. Osteikoetxea, O. Østergaard, M. Ostrowski, J. Park, D. M. Pegtel, H. Peinado, F. Perut, M. W. Pfaffl, D. G. Phinney, B. C. Pieters, R. C. Pink, D. S. Pisetsky, E. Pogge Von Strandmann, I. Polakovicova, I. K. Poon, B. H. Powell, I. Prada, L. Pulliam, P. Quesenberry, A. Radeghieri, R. L. Raffai, S. Raimondo, J. Rak, M. I. Ramirez, G. Raposo, M. S. Rayyan, N. Regev-Rudzki, F. L. Ricklefs, P. D. Robbins, D. D. Roberts, S. C. Rodrigues, E. Rohde, S. Rome, K. M. Rouschop, A. Rughetti, A. E. Russell, P. Saá, S. Sahoo, E. Salas-Huenuleo, C. Sánchez, J. A. Saugstad, M. J. Saul, R. M. Schiffelers, R. Schneider, T. H. Schøyen, A. Scott, E. Shahaj, S. Sharma, O. Shatnyeva, F. Shekari, G. V. Shelke, A. K. Shetty, K. Shiba, P. R. Siljander, A. M. Silva, A. Skowronek, O. L. Snyder, R. P. Soares, B. W. Sódar, C. Soekmadji, J. Sotillo, P. D. Stahl, W. Stoorvogel, S. L. Stott, E. F. Strasser, S. Swift, H. Tahara, M. Tewari, K. Timms, S. Tiwari, R. Tixeira, M. Tkach, W. S. Toh, R. Tomasini, A. C. Torrecilhas, J. P. Tosar, V. Toxavidis, L. Urbanelli, P. Vader, B. W. Van Balkom, S. G. Van Der Grein, J. Van Deun, M. J. Van Herwijnen, K. Van Keuren-Jensen, G. Van Niel, M. E. Van Royen, A. J. Van Wijnen, M. H. Vasconcelos, I. J. Vechetti, T. D. Veit, L. J. Vella, É. Velot, F. J. Verweij, B. Vestad, J. L. Viñas, T. Visnovitz, K. V. Vukman, J. Wahlgren, D. C. Watson, M. H. Wauben, A. Weaver, J. P. Webber, V. Weber, A. M. Wehman, D. J. Weiss, J. A. Welsh, S. Wendt, A. M. Wheelock, Z. Wiener, L. Witte, J. Wolfram, A. Xagorari, P. Xander, J. Xu, X. Yan, M. Yáñez-Mó, H. Yin, Y. Yuana, V. Zappulli, J. Zarubova, V. Žėkas, J. Zhang, Z. Zhao, L. Zheng, A. R. Zheutlin, A. M. Zickler, P. Zimmermann, A. M. Zivkovic, D. Zocco and E. K. Zuba-Surma, *J. Extracell. Vesicles*, 2018, 7, 1535750.